Eletrônica de Potência
Open Journal of Power Electronics

Received September 21, 2024; accepted February 04, 2025; Date of publication February 18, 2025.
The review of this paper was arranged by Associate Editor Montiê A. Vitorino and Editor-in-Chief Heverton A. Pereira.
Digital Object Identifier http://doi.org/10.18618/REP.e202520

Engine-Induction Generator Set Modeling for Hybrid/Flex Vehicle

Márcio V. R. Campos[1,*], Lucas J. R. Silva[1], Jen W. Wang[2], Thayson P. Alves[1], Bruno M. Zilli[1], Rodolpho V. A. Neves[3], Vilma A. Oliveira[1], Ricardo Q. Machado[1]

[1]University of São Paulo, Department of Electrical and Computer Engineering, Sao Carlos – SP, Brazil.
[2]Federal University of Sao Carlos, Department of Electrical Engineering, Sao Carlos, SP, Brazil.
[3]Federal University of Viçosa, Department of Electrical Engineering, Viçosa, MG, Brazil.

e-mail: marciovonrondow@usp.br*; lucasjonys@usp.br; jenwang@estudante.ufscar.br; a.thayson@usp.br; bruno.zilli@usp.br; rodolpho.neves@ufv.br; voliveira@usp.br; rquadros@sc.usp.br.
*Corresponding author

ABSTRACT This manuscript proposes a multiple-input, multiple-output (MIMO) model for an engine-induction generator set in series hybrid/flex vehicles (SHVs). The model outputs are simplified using linear combinations of the inputs via a steady-state gain matrix, with gains defined in terms of the SHV electrical parameters. A reduced-order model is proposed to reliably analyze the dynamic behavior by incorporating the state variables of the powertrain's electrical system. This facilitates the design of energy management systems (EMS) and power converter sizing, enhancing the efficiency of the engine-generator set. The mathematical solution was validated through simulations and experimental results, including mechanical power calculations derived from vehicle dynamics applied to an SHV laboratory-scale prototype. Experimental findings demonstrated the effectiveness of a simple EMS in reducing fuel consumption while maintaining the internal combustion engine within its optimal efficiency region. Furthermore, this study presents a practical and cost-effective alternative for ICE-generator systems by replacing permanent magnet synchronous generators (PMSGs) with induction generators (IGs).

KEYWORDS Hybrid/flex vehicles; ac/dc converter; three-phase induction generator; engine-generator set; circuit modeling; Hardware-in-the-Loop.

I. INTRODUCTION

Despite technological advancements, air pollution continues to pose a significant global challenge. Addressing this issue has become imperative as nations face mounting environmental pressures to reduce carbon dioxide (CO2) emissions.

In response, Brazil has initiated the MOVER 2030 program, which provides financial incentives to foster research, energy efficiency, and safety within the electric mobility sector. Among various sustainable solutions, series hybrid vehicles (SHVs) emerge as a promising alternative [1]. These vehicles offer reduced dependency on non-renewable fuels, lower fuel consumption, and decreased maintenance costs for consumers, aligning well with Brazil's vast highway network and reliance on road transport [2].

SHVs utilize as primary energy source an internal combustion engine (ICE) powered by gasoline or ethanol coupled with an electric generator to meet power demands, supplemented by energy storage devices such as electrolytic capacitors, supercapacitors, or batteries. These storage devices improve ICE efficiency while supporting transient power requirements during acceleration and deceleration phases. SHVs utilize gasoline or biofuel as their primary energy source, employing an internal combustion engine (ICE) coupled to an electric generator to meet the vehicle's power demands. Energy storage devices, such as electrolytic capacitors, supercapacitors, or batteries, are integrated to enhance ICE efficiency and support transient responses during vehicle acceleration and deceleration.

In this context, to ensure continuous power delivery from the electric generator to the storage elements, a three-phase rectifier is essential. In [3], three types of three-phase rectifiers were analyzed: an uncontrolled rectifier with diodes, a controlled rectifier with thyristors, and an ac/dc converter with pulse-width modulation (PWM) control. The study concluded that the ac/dc converter provides superior flexibility, reliability, and controllability, making it the most suitable power solution for SHVs.

Although the ac/dc converter is the optimal solution for electric mobility, its topology involves a large number of semiconductors. The quantity of semiconductors is directly proportional to the number of switching modes within a PWM cycle [4]–[6]. Consequently, modeling these converters dynamically, while accounting for the superposition of all switching modes during a PWM period, significantly increases computational complexity. This can delay simulations and hinder the timely execution of projects focused on control and energy management systems (EMS) [2].

In EMS, various strategies are employed to achieve optimal power sharing between the primary source and storage devices [7]. Data-driven control approaches, combined with deep reinforcement learning-based strategies as developed in [8], [9], eliminate the need for prior knowledge of the

converter's dynamic model. However, this lack of model dependency can impact the reliability of such designs concerning stability and safety. In contrast, EMS and control designs based on known dynamic models offer greater reliability by enabling precise observation of the state trajectories and control actions at specific operating points [10].

In this context, based on [11], [12], the authors in [2] developed a state-space model considering a permanent magnet synchronous generator (PMSG) with an ac/dc converter and a battery with a dc/dc converter, both connected to the dc-link of a SHV powertrain. The study aimed to reduce the complexity of implementing an EMS model for a fully active topology in SHV. However, the proposed model did not offer solutions for power control actions for the PMSG, specifically based on the phase angle and armature-applied voltage. Additionally, the model was applied exclusively for the PMSG and cannot be generalized to other generators, such as the three-phase induction generator.

In [13], the operational behavior and performance of self-excited induction generators (IGs) and PMSGs for small-scale isolated applications are compared. The study uses the same power source (a constant-speed prime mover) and load conditions (both resistive and inductive loads). Self-excitation and voltage regulation are experimentally investigated for IGs and compared to the performance of PMSGs. The findings suggest that both generators are suitable for small-scale isolated systems. However, if cost is not a constraint, PMSGs are recommended due to their ability to eliminate the need for additional capacitor arrangements for self-excitation and Volt-Ampere Reactive (VAR) compensation. Additionally, the use of PMSGs in SHVs is advantageous due to their efficiency, reliability, and compact, lightweight design, making them suitable for vehicle loads [14], [15].

Conversely, the authors in [13] concluded that IGs are preferable for cost-effective, small-size, flexible operation in both three-phase and single-phase modes, with enhanced reliability. Moreover, the efficiency and voltage regulation of IGs can be improved by specialized machine design and power electronic converters [16]. In this case, the need for additional capacitors for self-excitation and Volt-Ampere Reactive (VAR) compensation is eliminated. Therefore, considering the favorable cost-benefit ratio and the extensive body of literature on IGs [16]–[18], there is a clear need to investigate the energy generation subsystem of SHVs using IGs as the electric generator, in order to assess their performance and efficiency within the overall electrical powertrain.

To address these research gaps, this paper proposes a state-space model for an ICE-IG set and a battery connected to the dc-link in a semi-active topology SHV powertrain. The main objective is to enable designers to properly size the power converter and evaluate new control strategies for the SHV propulsion system using hardware-in-the-loop (HIL) simulations, as implemented in [19], or laboratory-scale setups, as demonstrated in this paper. The specific objectives of this work can be summarized as follows:

1) Simplify the multiple-input, multiple-output (MIMO) dynamic model to enable easier manipulation of transfer functions, as well as efficient calculation of equilibrium points and linearization;
2) Access the control inputs in the MIMO system to manage the rectified power from the IG in terms of frequency and the slip, which is associated with the control valve position of the ICE;
3) Make the MIMO model reliable for use in EMS and sizing projects for SHVs, ensuring good accuracy for HIL simulations while maintaining a low computational cost;
4) Emphasize the use of the ICE-IG set as a viable and cost-effective alternative for the power generation subsystem in low-power scale SHVs, offering a practical solution for energy generation in hybrid systems.

The paper is organized as follows: Section II presents the semi-active topology description and the ICE-IG set mapping efficiency; Section III presents the SHV powertrain modeling; Section IV presents the simulation results; Section V presents the experimental results obtained from a low-power scale prototype; and Section VI presents the conclusion.

II. SYSTEM DESCRIPTION

The series hybrid/flex electric architecture used in this work is illustrated in Figure 1. The topology is considered semi-active, where the battery is directly connected to the dc-link while a three-phase induction generator (TIG) is tied to the dc-link by using the power converter [20]. In this manner, the vehicle's propulsion system is fully electrified and powered by the dc-link, serving as the common energy-sharing point between sources and loads.

The energy flow is illustrated in Figure 1. As shown by the arrow directions, the battery can either absorb or supply energy to both the engine-generator set and the traction motors. The electric traction motors are capable of consuming power during vehicle operation and charging the storage elements in the dc-link during regenerative braking. This regenerative braking process enhances the vehicle's

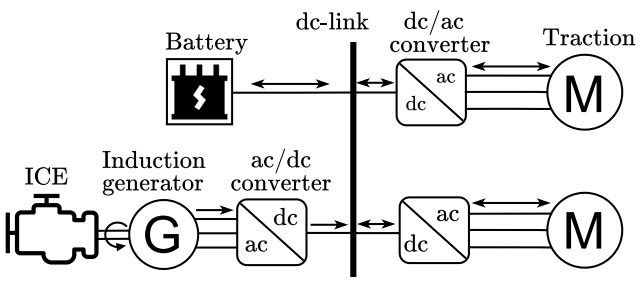

FIGURE 1. SHV architecture with the semi-active topology including a battery connected to dc-link, an ICE-IG set connecter to an ac/dc converter, and additional dc/ac converters used to drive the electric motors.

local efficiency, allowing for greater distances to be covered through energy recovery.

During the driving cycle, the engine-generator set continuously supplies energy to the storage elements, except during ICE startup scenarios, when assistance from the batteries is required to adjust the ICE speed through the generator. This ensures that the ICE operates within its optimal efficiency region, as illustrated in the generic efficiency map shown in Figure 2 [21], [22].

Therefore, as one of the objectives of this work is to reduce fuel consumption, an EMS is important to operate the ICE at the torque, speed, and power levels that maximize efficiency. In Figure 2, the curves generated by the combination of torque and speed illustrate the fuel consumption rate per kilowatt-hour (kWh) [21], [22]. This value decreases toward the nominal torque and speed point along the optimal operation line, where the ICE operates with maximum efficiency.

To ensure greater efficiency in converting mechanical to electrical energy, the TIG must be sized to match the nominal operating conditions of the ICE (rotational speed and torque levels). Thus, Figure 3(a) illustrates the operating region where the induction machine functions as an electric generator, i.e., when the rotor speed exceeds the machine's synchronous speed (frequency of the voltage applied to the stator), resulting in negative slip. Consequently, the negative slip generates negative torque to counterbalance the positive torque from the ICE, achieving static force equilibrium. Finally, the negative torque during rotor rotation generates electrical energy for the storage devices and propulsion system.

Based on the aforementioned ideas, Figure 3(a) illustrates the efficient generation region of the TIG, while Figure 3(b) depicts this region in terms of efficiency. The efficiency of the TIG decreases during no-load operations and at slip values far beyond its nominal range. Therefore, it is important to determine the lower and upper slip limits to optimize the conversion of mechanical energy into electrical energy. Subsequently, to achieve higher efficiency in the conversion of mechanical to electrical energy, it is advantageous to operate the TIG at synchronous speed and with slip values close to the nominal range.

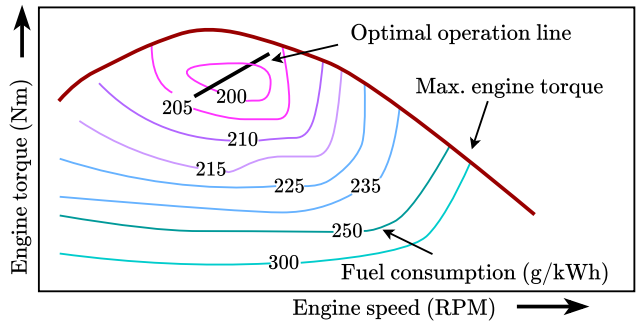

FIGURE 2. ICE fuel consumption per kilowatt-hour in terms of torque and speed.

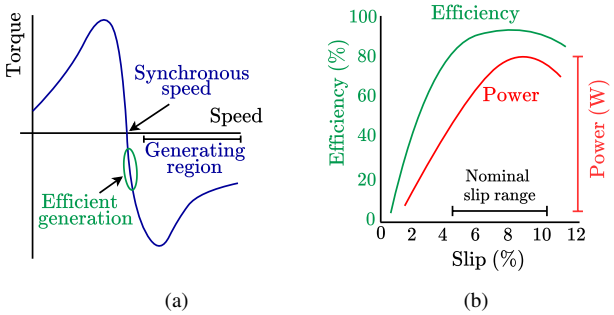

FIGURE 3. (a) Torque vs rotor speed for TIG, highlighting the generating region. (b) TIG efficiency and power, highlighting the nominal slip range in efficient generation region.

III. PROPOSED MODELING FOR A HYBRID/FLEX VEHICLE

An analytical understanding of the model facilitates the design of the engine-generator set to operate more efficiently in SHV solutions with varying electrical characteristics. This work presents a study on modeling the hybrid system based on the powertrain semi-active topology shown in Figure 4, with a focus on the energy generation subsystem.

The battery terminals are connected to the dc-link through an inductor filter, which flows the instantaneous current i_{batt}. The engine-inductor generator set is tied to the dc-link by a bidirectional ac/dc converter, where i_k is the instantaneous phase currents extracted from the TIG and d_k the instantaneous duty-cycles applied to the ac/dc converter, for $k \in \{1, 2, 3\}$.

Additionally, the dc-link processes the average output current of the battery i_{batt}, the ac/dc current i_ϕ, the current flowing through the load R and the average vehicle power/current i_o subjected to the instantaneous dc-link voltage v_o on the capacitance C_o.

Based on the powertrain description, the mathematical model of the overall electrical topology is developed as a multiple-input multiple-output (MIMO) system using the average state-space modeling technique.

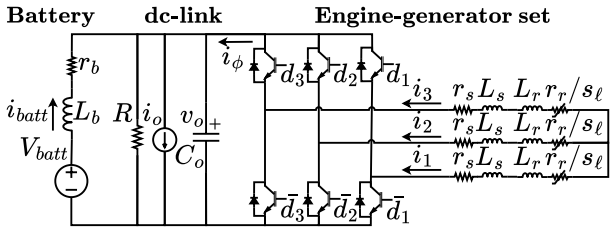

FIGURE 4. Semi-active topology variables used, with battery direct linked on the dc-link and the ICE-IG set voltage regulator, which includes an ac/dc converter.

A. Modeling of inductor currents

The dynamics of the battery inductor current is given by

$$\dot{i}_{batt} = -\frac{r_b}{L_b} i_{batt} - \frac{v_o}{L_b} + \frac{V_{batt}}{L_b} \tag{1}$$

where V_{batt} is the battery terminal voltage input and i_{batt} is the instantaneous current, filtered by the inductance L_b and its parasitics losses r_b.

In the same way, the currents i_k with $k \in \{1, 2, 3\}$ extracted from the TIG can be derived from the differential equations based on the induction generator equivalent circuit [11]:

$$\dot{i}_k = -\left(\frac{r_s}{L_f} + \frac{r_r}{s_\ell L_f}\right) i_k - \frac{v_o}{L_f} d_k, \tag{2}$$

$$d_k = \frac{0.85f}{2f_{max}} \sin\left(\omega_f t - \frac{2(k-1)}{3}\pi\right) \tag{3}$$

where L_f is the sum between the stator inductance L_s and rotor inductance L_r while the rotor and stator losses are given by r_r and r_s, respectively. The duty-cycles $d_k \in [-0.85, 0.85]$ are calculated to establish a linear relationship between the phase terminal voltage and the machine synchronous frequency f, while f_{max} is the maximum synchronous frequency and $\omega_f = 2\pi f$ represents the machine angular velocity. Finally, s_ℓ represents the machine slip, which is related to the torque produced by the TIG for power generation.

Subsequently, solving the differential equation in (2), the instantaneous currents i_k, neglecting the initial transient response, are calculated according to

$$i_1 = \frac{\alpha_1 L_f s_\ell \omega_f \cos(\omega_f t)}{\beta_1} - \frac{\alpha_1 (r_r + r_s s_\ell) \sin(\omega_f t)}{\beta_1}, \tag{4}$$

$$i_2 = \frac{\alpha_1 (r_r + r_s s_\ell)}{\beta_1} \sin(\pi/3 + \omega_f t) - \ldots \\ \ldots - \frac{\alpha_1 L_f s_\ell \omega_f \cos(\pi/3 + \omega_f t)}{\beta_1}, \tag{5}$$

$$i_3 = -\frac{\alpha_1 (r_r + r_s s_\ell)}{\beta_1} \sin(\pi/3 - \omega_f t) - \ldots \\ \ldots - \frac{\alpha_1 L_f s_\ell \omega_f \cos(\pi/6 + \omega_f t)}{\beta_1} \tag{6}$$

where

$$\alpha_1 = v_o \frac{0.85f}{2f_{max}} s_\ell \text{ and } \beta_1 = (L_f s_\ell \omega_f)^2 + (r_r + r_s s_\ell)^2.$$

Therefore, the average output current of the ac-dc converter i_ϕ is given by

$$i_\phi = i_1 d_1 + i_2 d_2 + i_3 d_3. \tag{7}$$

Finally, the average current i_ϕ is achieved by substituting (3), (4), (5), and (6) in (7), which yield

$$i_\phi = -v_o \left(\frac{0.85f}{f_{max}}\right)^2 \frac{3 s_\ell (r_r + r_s s_\ell)}{8\beta_1}. \tag{8}$$

B. Modeling of dc-link voltage

To couple the power converter and loads connected to the dc-link, the contribution of each current flowing through the common coupling point, as shown in Figure 5, results in the dc-link voltage dynamics as follows:

$$\frac{dv_o}{dt} = \frac{i_{batt}}{C_o} + \frac{i_\phi}{C_o} - \frac{v_o}{RC_o} - \frac{i_o}{C_o} \tag{9}$$

In steady-state regime, considering the equilibrium operation, $\dot{v}_o = 0$, the dc-link average voltage can be determined as follows:

$$V_o = (I_{batt} - I_o)\, \beta_2 \tag{10}$$

where

$$\beta_2 = \frac{8\beta_1 f_{max}^2 R}{2.17 R s_\ell (r_r + r_s s_\ell) f^2 - 8\beta_1 f_{max}^2},$$

I_o the constant current from the vehicle load, and I_{batt} is the average current that flows by the battery, which is obtained replacing (10) in (1), assuming $\dot{i}_{batt} = 0$:

$$I_{batt} = \frac{V_{batt}}{r_b + \beta_2} + \frac{I_o \beta_2}{r_b + \beta_2}. \tag{11}$$

In this manner, the dc-link voltage gain and the battery current can be analyzed in steady-state regime based on the TIG operation points.

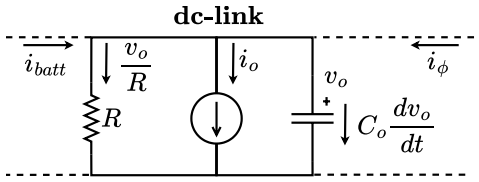

FIGURE 5. Currents flowing over the dc-link coupled by the dc/dc and ac/dc bidirectional converters.

C. State-space average model and static gain

The state-space model is obtained using (1), (9) and (8), defining the input vector $\boldsymbol{u} = [V_{batt}\ i_o]^T$, the state vector $\boldsymbol{x} = [i_{batt}\ v_o]^T$ and the output vector $\boldsymbol{y} = [i_{batt}\ v_o\ i_\phi]^T$. Additionally, the authors are able to calculate $\boldsymbol{A} \in \mathbb{R}^{2\times2}$, $\boldsymbol{B} \in \mathbb{R}^{2\times2}$, and $\boldsymbol{C} \in \mathbb{R}^{3\times2}$, represented by

$$\begin{cases} \dot{\boldsymbol{x}} = \boldsymbol{A}\boldsymbol{x} + \boldsymbol{B}\boldsymbol{u} \\ \boldsymbol{y} = \boldsymbol{C}\boldsymbol{x} \end{cases} \tag{12}$$

where $\boldsymbol{A}$, $\boldsymbol{B}$ and $\boldsymbol{C}$ are matrices dependent of the electrical circuit parameters, given by

$$\boldsymbol{A} = \begin{bmatrix} -\frac{r_b}{L_b} & -\frac{1}{L_b} \\ \frac{1}{C_o} & \left(-\left(\frac{0.85f}{f_{max}}\right)^2 \frac{3 s_l (r_r + r_s s_l)}{8\beta_1 C_o} - \frac{1}{RC_o}\right) \end{bmatrix}, \tag{13}$$

$$\boldsymbol{B} = \begin{bmatrix} \frac{1}{L_b} & 0 \\ 0 & -\frac{1}{C_o} \end{bmatrix}, \tag{14}$$

$$\boldsymbol{C} = \begin{bmatrix} 1 & 0 \\ 0 & 1 \\ 0 & -\left(\frac{0.85f}{f_{max}}\right)^2 \frac{3 s_l (r_r + r_s s_l)}{8\beta_1} \end{bmatrix}. \tag{15}$$

To analyze the steady-state under different operating conditions, the static-gain is obtained. Therefore, using the matrices described in (13), (14) and (15), and assuming that the power-plant is working in steady-state as $\boldsymbol{X} = \boldsymbol{x}(\infty)$, $\boldsymbol{U} = \boldsymbol{u}(\infty)$ e $\boldsymbol{Y} = \boldsymbol{y}(\infty)$, that is, $\dot{\boldsymbol{X}} = 0$:

$$\begin{cases} \boldsymbol{X} = -\boldsymbol{A}^{-1}\boldsymbol{B}\boldsymbol{U} \\ \boldsymbol{Y} = -\boldsymbol{C}\boldsymbol{A}^{-1}\boldsymbol{B}\boldsymbol{U} \end{cases}, \tag{16}$$

the static gain matrix is obtained using (16), resulting in

$$\boldsymbol{G} = -\boldsymbol{C}\boldsymbol{A}^{-1}\boldsymbol{B}, \tag{17}$$

where the elements of $\boldsymbol{G}$, denoted G_{ij}, are presented in Table 1.

TABLE 1. Matrix elements of G.

G_{11}	$\dfrac{\sigma_1 + R\sigma_2}{r_b\sigma_1 + R(\sigma_1 + r_b\sigma_2)}$	G_{12}	$\dfrac{R\sigma_1}{r_b\sigma_1 + R(\sigma_1 + r_b\sigma_2)}$
G_{21}	$\dfrac{R\sigma_1}{r_b\sigma_1 + R(\sigma_1 + r_b\sigma_2)}$	G_{22}	$\dfrac{-Rr_b\sigma_1}{r_b\sigma_1 + R(\sigma_1 + r_b\sigma_2)}$
G_{31}	$\dfrac{-R\sigma_2}{r_b\sigma_1 + R(\sigma_1 + r_b\sigma_2)}$	G_{32}	$\dfrac{Rr_b\sigma_2}{r_b\sigma_1 + R(\sigma_1 + r_b\sigma_2)}$

$$\sigma_1 = 8f_{max}^2\left(\omega_f^2 L_s^2 s_\ell^2 + \beta_1\right)$$
$$\sigma_2 = 3(0.85f)^2(r_r s_\ell + r_s s_\ell^2)$$

IV. SIMULATION RESULTS

In this section, the model in (12), treated as a MIMO system, will be validated as in [2], [5]. To achieve this, MATLAB/SIMULINK software is utilized, with the electrical parameter values for the SHV powertrain in the laboratory-scale prototype provided in Table 2. The parameters of the laboratory-scale prototype used to emulate the vehicle and, consequently, the load on the dc-link is presented in Table 3.

A. Validation of the average model

The responses of the switched circuit are compared with those obtained from (12). The switched electrical circuit was developed using SIMULINK, while (12) was solved by the Runge-Kutta toolbox in MATLAB. The simulation was conducted with fixed time steps of 10^{-6} seconds.

A vehicle load profile i_o, was extracted from the New European driving cycle, considering vehicle dynamics along with aerodynamic and rolling losses [23]. Additionally, the responses from (12) and the simulated switched circuit are displayed in Figure 6. It is evident that the dynamic response of the simplified model follows the dynamics of the switched circuit.

The average errors between the theoretical model and the simulated switched circuit for i_{batt}, i_ϕ and v_o are 0.025 A, 0.022 A and 0.10 V, respectively. The percentage error with respect to the root mean square (RMS) values of i_{batt}, i_ϕ and v_o are 4.12%, 5.45% and 0.03%, respectively. This relative error is attributed to the sampling time used in the switched model, which impacts the processing time for calculating the outputs. Although the models exhibit errors around 5% in i_ϕ, it can still be inferred that the simplification provides good accuracy compared to the more complex and computationally demanding switched model.

TABLE 2. Laboratory scale prototype parameters.

	Parameter	Value
Battery	Rated current	1 Ah/5 A @ 5C
	Rated voltage (V_{batt})	310 V
	L_b	5 mH
	r_b	100 mΩ
TIG WEG (W22 IR3)	Rated voltage/current	220 Vrms/1.25 Arms
	Nominal velocity	3,600 RPM @ 2 poles
	Rated/peak power	500 W/1,000 W
	Efficiency/slip	>77%/5%
	$L_r = L_s$	50 mH*
	r_s	8.32 Ω*
	r_r	6 Ω*
dc-link	Min./max. v_o	260 V/410 V
	R	400 Ω
	C_o	1,000 μF
ac-dc converter (CFW300)	Rated/max. power	800 W/2,200 W
	Efficiency	>90%
	f_{max}	60 Hz
	f_s	10 kHz

* Parameters estimated at a nominal speed of 3,440 RPM.
f_s: Switching frequency.

B. Static gain matrix

The static gains graphs are plotted to assess the influence of the synchronous speed and the slip of the engine-induction generator set given by the mathematical model gains presented in Table 1. Figure 7 displays the gains variation as a function of the TIG synchronous frequency f in the range $[25\ \ 35]$ Hz and the slip s_ℓ in the range $[-1\ \ 0]$, while the other electrical parameters were kept constant according to the values in Table 2. For G_{ij}, the rows $i \in 1, 2, 3$ correspond to the outputs i_{batt}, v_o, and i_ϕ, respectively, while the columns $j \in 1, 2$ are associated with the inputs V_{batt} and i_o, respectively.

TABLE 3. SHV Laboratory-scale prototype parameters.

Parameter	Value
Machine type	Three phase induction motor (WEG - W22 IR3)
Rated voltage	220 Vrms
Rated/max. current	1.18 Arms/2.27 Arms
Rated/max. power	250 W/500 W
Nominal velocity	3,600 RPM @ 2 poles
Efficiency/slip	>73%/6%

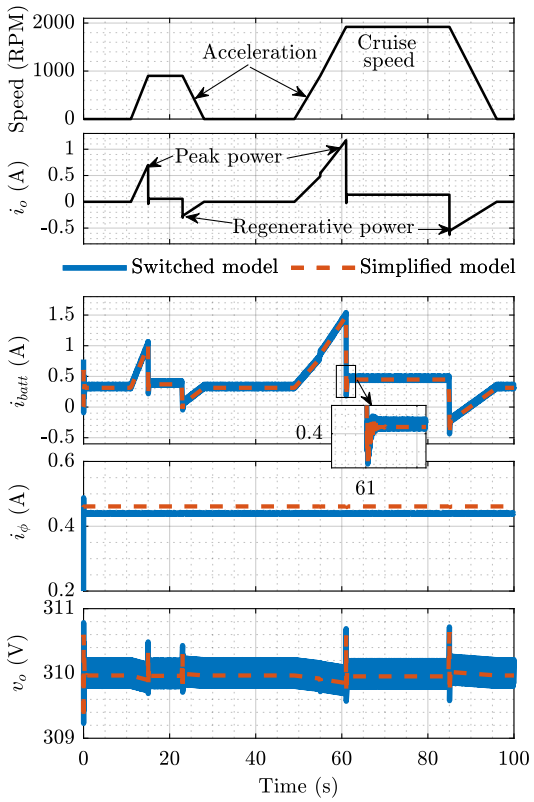

FIGURE 6. Vehicle speed and dc-link current load. Additionally, the variables output of the theoretical model was compared to a simulated switched circuit.

For all combinations of s_ℓ and f, $G_{11} \approx 0$ and $G_{12} \approx 1$, indicating that the input i_o has a greater influence on the output i_{batt} than V_{batt}. This is due to the direct connection of the battery to the dc-link, which allows the storage unit to supply the remaining vehicle load demand, given that the load provided by the engine-generator set remains constant for all selected combinations.

On the other hand, $G_{21} \approx 1$ indicates a strong relationship between v_o and V_{batt} due to the direct connection of the battery terminals to the dc-link in the semi-active topology. Additionally, $G_{22} \approx -0.1$ shows that load variations can significantly impact the steady-state value of v_o for magnitudes of i_o greater than 10 A. However, the load handled by the vehicle prototype is of low magnitude (low power scale), resulting in minimal disturbance to v_o.

Although the gains G_{31} and G_{32} are low, the final output i_ϕ is significantly influenced by V_{batt}, which exhibits high values due to the use of the dc-link. This is because V_{batt} affects v_o, and the rectified output i_ϕ depends on the high dc-link voltage. Furthermore, for the vehicle prototype with the components listed in Tables 2 and 3, the load $i_o < 1$ A does not influence the output i_ϕ, since $G_{32} \approx 0$.

Finally, it is noted that G_{31} experiences an increase in gain for higher f and for $s_\ell \approx 0.25$, indicating that more power from the engine-generator set will be delivered to the vehicle. However, this operation requires a high slip, which may lead to inefficiencies in electrical energy conversion and, consequently, in fuel economy.

To validate the steady-state analysis of the MIMO system, the switched circuit was simulated for different combinations of f, s_ℓ and i_o. The results obtained were compared with the predicted steady-state values based on the gains of $\boldsymbol{G}$. To simplify the analysis, a constant load profile i_o was used, representing a steady-state load regime during the vehicle cruising speed.

As shown in Figure 8, the outputs of the switched circuit reach the steady-state values predicted by the model in (16) while the quantitative results are presented in Table 4. The quantitative results showed a low relative error between the outputs of the simplified model and the switched model, supporting the reliability and accuracy of the analyzed model.

The average output current of the ac/dc converter is highly dependent on f and s_ℓ, which, in turn, affects the resistive torque of the TIG on the combustion engine coupled to its rotor. As f approaches 60 Hz, the TIG exhibits improved efficiency and performance, increasing the power injected into the dc-link. This power can be controlled by selecting s_ℓ within the machine's rated range. Although the supplied power is higher at greater slips, the TIG experiences high overload and reduced efficiency. Therefore, it is recommended to use slip values below 10%, as suggested by the technical specifications.

TABLE 4. Theoretical model outputs and the error in relation to the simulated switched model.

	$f = 30$ Hz $s_\ell = -0.1$ $i_o = 0.5$ A	Error (%)	$f = 35$ Hz $s_\ell = -0.2$ $i_o = -0.9$ A	Error (%)
i_{batt} (A)	0.94	1.05	-0.66	0.51
v_o (A)	309.91	0.01	310.07	0.03
i_ϕ (A)	0.34	4.61	0.54	0.2

V. EXPERIMENTAL RESULTS

The experimental tests to validate the proposed model were conducted on a laboratory-scale prototype, as illustrated in Figure 9. The prototype's electrical parameters for both the energy generation and vehicle traction subsystems are provided in Tables 2 and 3, respectively.

Engine-generator set emulation: A pair of three-phase induction machines was used to emulate the engine-generator set, where the internal combustion engine is represented by a three-phase induction motor (TIM) and the electric generator is represented by a TIG. Each machine has a dc/ac converter for speed control via analog commands. The operating principle consists of using the TIG to control the speed on the coupling shaft of the machines at the reference f_g through a closed-loop vector control. Coupled to this shaft, the TIM adjusts its synchronous speed f_c using open-loop V/f control. The difference between f_c and f_g induces a slip in the TIG, which determines the torque effect and

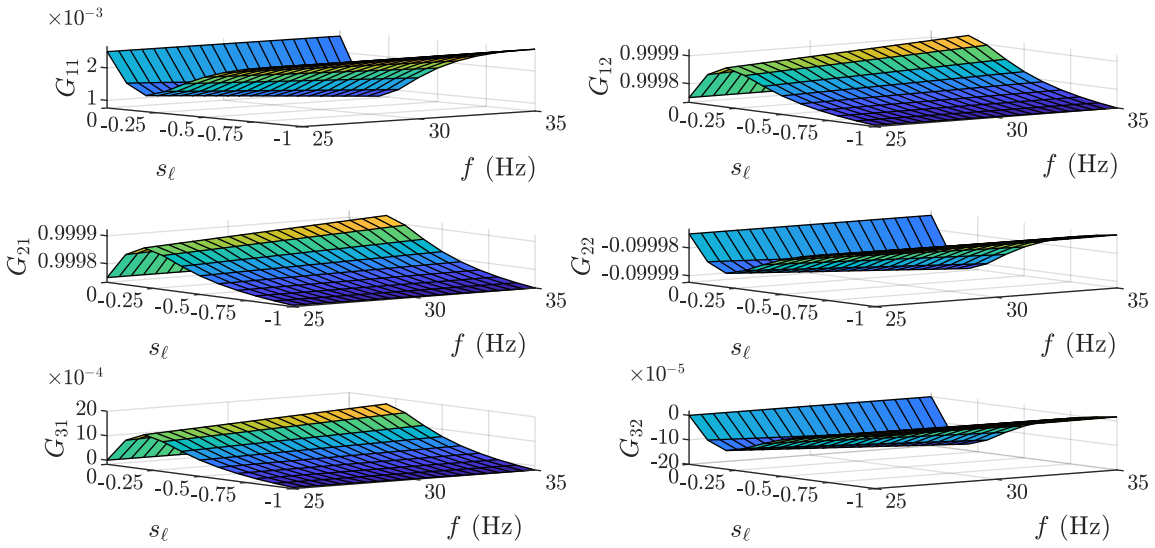

FIGURE 7. Influence of the TIG slip and its synchronous frequency, according to the static gain matrix.

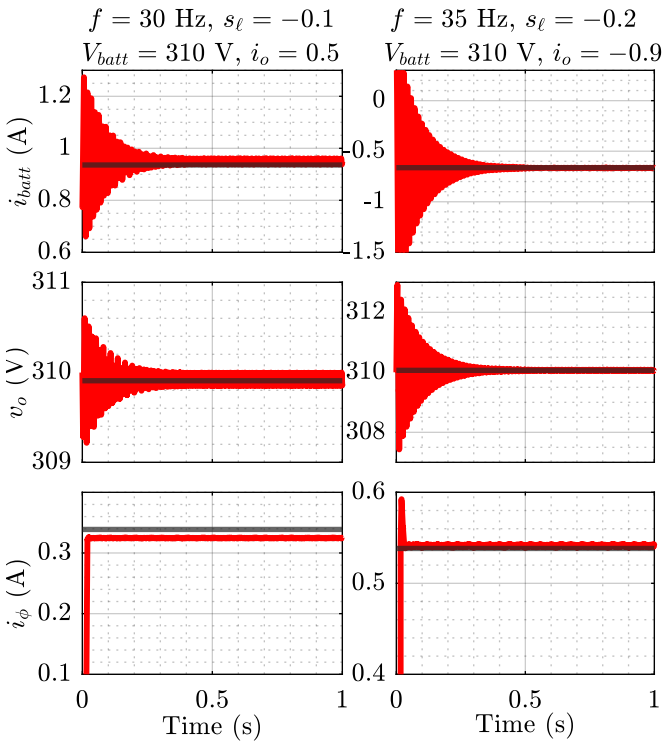

FIGURE 8. Comparison of the switched circuit response with the model prediction using the static gain matrix for different combinations of f, s_ℓ and i_o. The red line represents the output of the switched circuit, while the black line represents the theoretical model prediction based on the Table 1.

consequently changes the power processed by the electric generator as follows:

$$\begin{cases} s_\ell < 0 \text{ and } i_\phi > 0, & f_c > f_g \\ s_\ell \geq 0 \text{ and } i_\phi \leq 0, & f_c \leq f_g \end{cases} . \tag{18}$$

Therefore, the angular position of the accelerator pedal can send a reference signal to adjust f_c, introducing slip in the TIG and thereby emulating the power transfer of the engine-generator set.

Vehicle load emulation: To emulate the vehicle load, two pairs of three-phase induction machines were coupled as well. In each pair, one machine operates as a propulsion motor while the other emulates the vehicle resistive forces (inertia and aerodynamic drag). The operating principle is similar to that of the energy generation unit, where each machine is connected to a dc/ac converter that receives analog signals for controlling its speed and torque.

The synchronous speed difference between the coupled machines determines the slip and torque (T_{tr}) applied by the propulsion system. When the synchronous speed of the resistive machine (f_{rs}) is lower than that of traction (f_{tr}), the vehicle consumes energy (in scenarios of acceleration and cruising speed); otherwise, regenerative energy production occurs (in braking scenarios). Thus, the vehicle load emulation can be empirically estimated using the following mathematical approximations:

$$\begin{cases} i_o \propto T_{tr} f_{tr} \geq 0, & f_{tr} \geq f_{rs} \\ i_o \propto T_{tr} f_{tr} < 0 & f_{tr} < f_{rs} \end{cases} . \tag{19}$$

Thus, f_{rs} can be determined in terms of f_{tr} based on the vehicle dynamics equations, as follows:

$$\begin{cases} \dot{f}_{tr} = \frac{1}{J}\left(p_{acc}\gamma - p_{bk}\gamma - f_{tr}\right) \text{ with} \\ f_{rs} = f_{tr} - \alpha J \dot{f}_{tr} - C_{dg} f_{tr}^2, \; p_{acc} || p_{bk} > 0 \\ f_{rs} = f_{tr}, \text{ otherwise} \end{cases} \tag{20}$$

where J and C_{dg} are the inertia and drag coefficients of the prototype vehicle, p_{acc} and p_{bk} are the accelerator and brake pedal pressure normalized (0 to 1), while α and γ are unit conversions. Therefore, after calculating f_{rs}, it is normalized

to be sent as a control signal to the dc/ac converters of the coupled machines.

Finally, two pedals were utilized to emulate the vehicle's accelerator and brake. In this test bench setup, the accelerator and brake pedals send reference signals to control the machine synchronous speeds.

Battery emulation: To emulate the battery, a bidirectional programmable power supply model manufactured by Itech Electronics was used. This power supply is embedded with software that allows the emulation of an energy storage system, enabling the configuration of parameters such as minimum/maximum current, voltage, state of charge, and energy capacity in Ah. The power supply terminals were directly connected to the dc-link via an inductor, while the TIG was connected to the dc-link through the ac/dc converter.

Remark 1:
Although the battery dynamics were not considered in the modeling, its non-linearities were taken into account in the experimental results. The battery terminal voltage was not constant, being defined as a function of its state-of-charge. However, the state of charge did not change significantly in the experimental results.

Electronic Control Unit: The control commands that generate the speed references for the machines were developed in SIMULINK on the host computer. Subsequently, the program was compiled and integrated into the dSPACE MicroAutoBox II. This device is used as the electronic control unit (ECU) of the system and has an integrated graphical interface on the host computer, where real-time reading of current and voltage signals measured by the sensors is performed, along with data recording, filtering, and exporting.

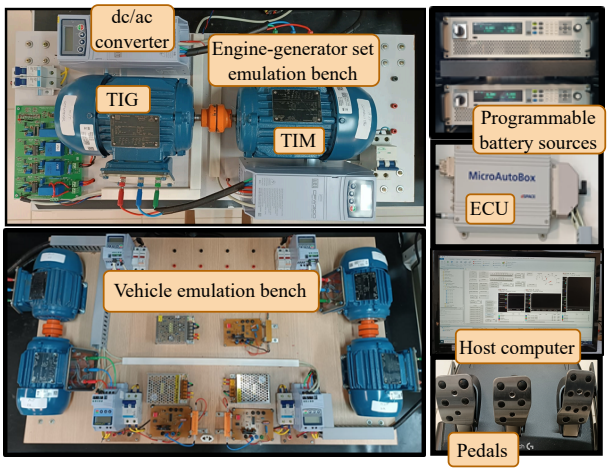

FIGURE 9. Laboratory-scale SHV prototype along with bench devices for testing and experimentation.

A. Theoretical model validation

The theoretical model of the average current i_ϕ as in (8) was validated by comparing the average power generated with the experimental data collected from the generation subsystem prototype shown in Figure 9. The results were compared under different operating conditions by systematically varying f and s_ℓ in both the theoretical model and the TIG of the experimental bench.

In order to increase the accuracy of the theoretical model with experimental data, (8) was adjusted by modifying the inductance L_s with a magnetic saturation coefficient, which exhibits non-linear behavior at low frequencies. Magnetic saturation occurs when the magnetic flux exceeds the core material's capacity to store it linearly, altering the nominal inductance value of the machine [24].

Thus, measurements of the machine's magnetizing current were taken at different frequencies, which allowed the empirical formulation of the following mathematical model for the saturation coefficient:

$$k_{sat} = \frac{1}{1 + c_\alpha e^{c_\beta (f_\gamma - f_g)}}, \tag{21}$$

where c_α, c_β, and f_γ are parameters estimated based on experimental data. Thus, the new inductance used in (8) is expressed as follows:

$$L_{new} = L_s / k_{sat}. \tag{22}$$

As shown in Figure 10, the theoretical model demonstrated similarity with the experimental data. The behavior of k_{sat} in (21) closely matched the experimental data, while the machine power results for different frequencies and slips showed average errors below 3%.

However, the model still does not account for variations in core loss and rotor resistance at low frequencies, which may impact the energy efficiency analysis in these operating regions. Given that the TIG operates far from these frequencies, these effects become negligible in (8). Nevertheless, to achieve a high precision model suitable for robust controller designs, it is necessary to incorporate a state observer in (12) using a Kalman filter, as implemented in [25], and to estimate parameters across a wider range of operating frequencies, which can be achieved through meta-heuristic optimization techniques, as presented in [26].

B. Engine-generator set energy management

A simple power control method was implemented using the laboratory-scale prototype, where pedal pressure generates torque reference for the traction motors and the combustion engine simultaneously. In this way, the vehicle starts to move while the primary source supplies the required power. The batteries in the dc-link act as auxiliary sources to meet the high-frequency demands in the vehicle responses, such as sudden accelerations and braking.

In Figure 11, the schematic to generate the traction torque command s and the slip signals to the TIG is exhibited. The

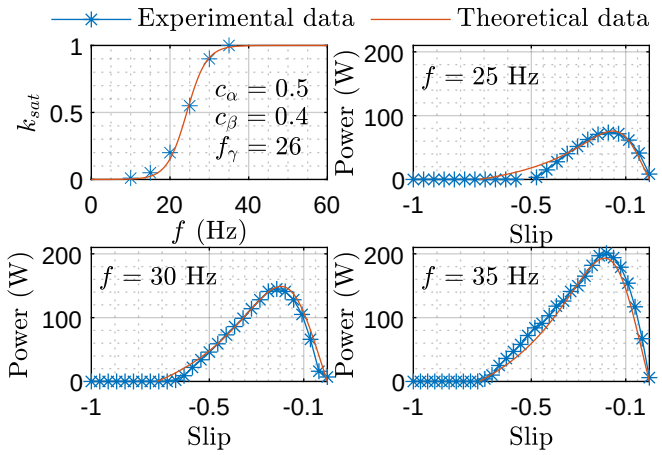

FIGURE 10. Comparison between the experimental data obtained on the test bench (Figure 9) and the theoretical data obtained from (8) and (21) for different synchronous frequencies.

pedal pressure gives the reference signal u_α to speed-up the vehicle and increase the combustion engine ignition.

The pedal pressure affects the angular position of the throttle valve in the carburetor. This valve increases the flow of the ignition mixture, increasing the torque produced by the ICE. Thus, the dynamics of this process was simplified to a low-pass filter $LPF(s)$ with gain k_α, where the output signal is the slip $s_{\ell\alpha}$. Additionally, $s_{\ell\alpha}$ is added to the initial slip $s_{\ell o}$, which constantly acts on the TIG. The sum of $s_{\ell\alpha}$ and $s_{\ell o}$ corresponds to the reference slip $s_{\ell_{ref}}$, which is used to generate the rectified current i_ϕ, adjusted in terms of the synchronous frequency f and s_ℓ.

In this context, Figure 12 presents the data collected from the energy management test of the engine-generator set on the laboratory-scale prototype, as well as the theoretical data extracted from the model in (12). It shows, from top to bottom: the behavior of the pedal pressures for the throttle and brake; $s_{\ell\alpha}$ given by the synchronous frequency difference of the induction machine emulating the combustion engine and the electric generator; the rotational frequency of the induction machines emulating the traction and resistance of the vehicle prototype; the power processed by the engine-generator set (P_{ge}) and by the batteries (P_{batt}); and lastly, the dynamics of the voltage on the dc-link.

The throttle and brake pressures adjust the speed of the vehicle propulsion machines according to the first-order system. As shown in Figure 12, the frequencies f_{tr} and f_{rs}

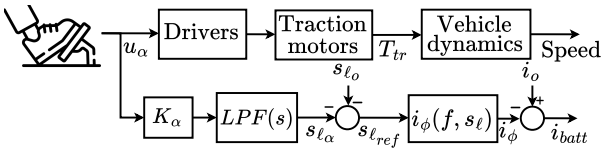

FIGURE 11. EMS designed to share power between the battery and the ICE-IG set based on vehicle load demands.

are calculated according to (20), defining the load power to be extracted from the vehicle prototype as described in (19).

Additionally, the accelerator pressure influences the slip $s_{\ell\alpha}$ due to the frequency mismatch between the internal combustion engine f_c and the electric generator f_g. As expected, increasing or decreasing $s_{\ell\alpha}$ makes the induction generator power to be injected to compensate the load demand requested at the dc-link terminals of the prototype.

Therefore, the power produced P_{ge} and P_{batt}, as well as the v_o dynamics were validated against the ordinary differential equations (ODEs) in (12). For this purpose, $s_{\ell\alpha}$ and i_{load}, extracted from experimental tests, were used as inputs in the ODEs, with the solution performed using the Runge-Kutta method (ODE45) in MATLAB.

As shown in the comparisons presented in Figure 12, the responses obtained from the theoretical model match with the experimental results, corroborating the model reliability in representing the energy conversion performed by the proposed ac/dc converter in the described topology. The observed differences are due to model simplifications and sensor calibration. The error is more pronounced in v_o results, where the experiments revealed greater oscillation and response to load-induced disturbances. This can be attributed to internal losses inherent to the source emulating the battery and parasitic losses r_b, which were not accurately represented in the theoretical model.

C. Efficiency analysis

This section discuss the advantages and disadvantages between a TIG and a PMSG, both marketed by E-Comer, with the goal of identifying the best design trade-off by analyzing efficiency, power density, practicality, and cost.

Figures 13(a) and 13(b) show the efficiency maps of the TIG and PMSG, respectively, as reported in Table 5. It can be observed that the PMSG exhibits superior efficiency over a wide range of speed and torque compared to the TIG. The high efficiency of the PMSG is expected due to the absence of losses associated with the excitation of the magnetic field. The TIG, on the other hand, has core losses due to the excitation of the magnetic field, which impact its performance under partial load conditions.

For the TIG to operate with high efficiency, it is necessary to develop an EMS that keeps it within the nominal speed and torque range for most of the time, which is more restrictive compared to the PMSG. For this reason, the EMS in this paper was developed to operate the machine at nominal speed with an average torque of 30% of the maximum value (T_{max}). This allowed the generator to operate in the region of highest efficiency and achieve performance comparable to the PMSG.

Although the PMSG outperforms the TIG over a wider range of speed and torque, it requires specialized materials and electrical components, which can increase both the complexity and cost of the design. As shown in Table 5, the PMSG exhibits superior power density. However, its

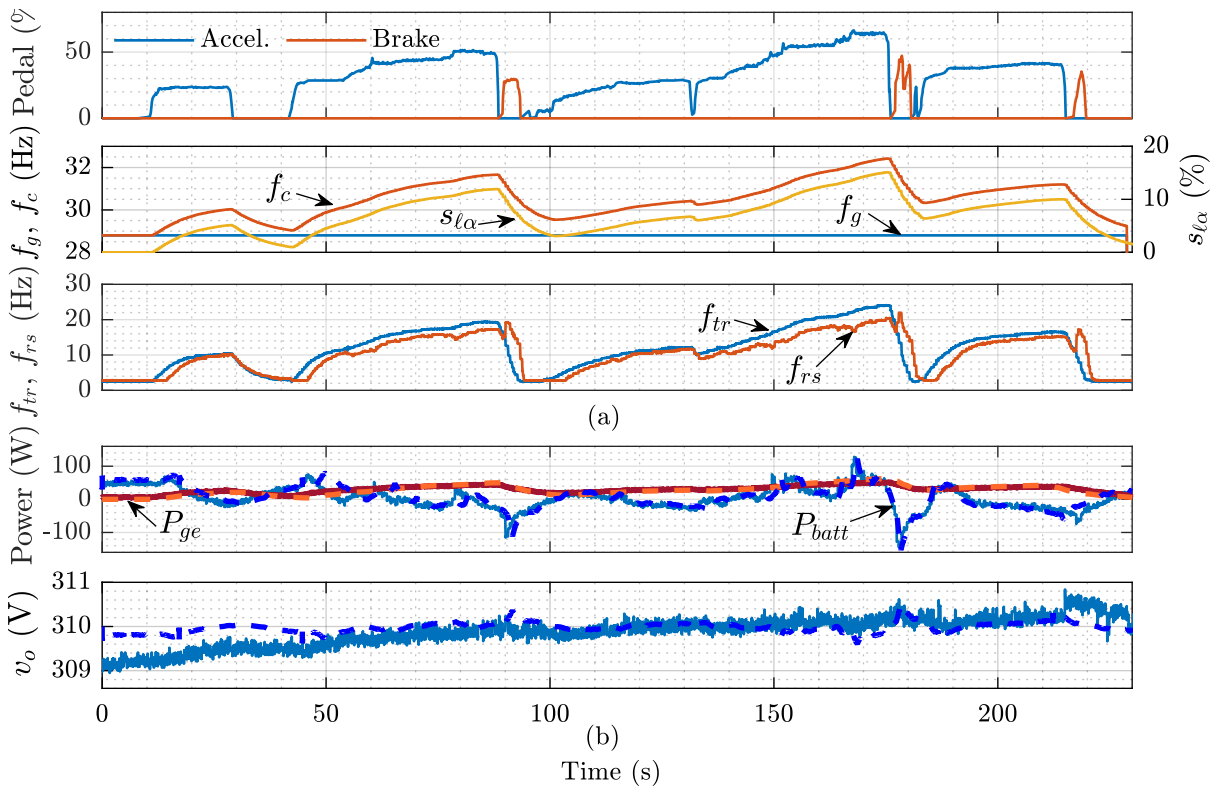

FIGURE 12. Results collected from the test bench and from the theoretical model. (a) Measurements of the engine-generator set and vehicle load emulation in the test bench. (b) Results from the test bench (continuous line) compared to the results of the theoretical model (dashed line).

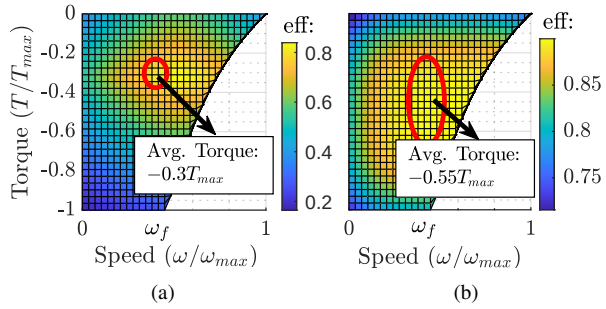

FIGURE 13. Efficiency map: (a) TIG and (b) PMSG.

TABLE 5. E-Comer electric machine comparison.

Model	Power	Weight	Rot./freq.	Voltage	Avg. Cost
TIG AMAC 200-125	13 kW	30 kg	3000 rpm/ 103 Hz	68 Vrms	US$ 2.000
PMSG SMAC 200-035	12 kW	25 kg	3500 rpm/ 233 Hz	68 Vrms	US$ 3.000

acquisition cost is higher due to the specific materials used in its construction. Additionally, the PMSG features a greater number of poles, which increases the switching frequency of the ac/dc converter, thereby raising the complexity of designing the converter topology.

The TIG, being a well-established component in the literature and in the Latin American market, presents a viable alternative for prototype-level projects, focusing on cost reduction, simplification, and practicality in the implementation of EMS. This work aims to highlight these advantages by developing static and dynamic models to reduce the complexity of control systems in TIGs using AC/DC converters, specifically for application in energy generation subsystems for SHVs.

VI. CONCLUSION

In this paper, a simplified power transfer model from an engine-generator set by considering an IG rectified by an ac/dc converter for hybrid vehicles is proposed. The power transfer equations were formulated in terms of the slip of the three-phase induction generator, with the goal of compensating for the torque required by the internal combustion engine, which was emulated by a TIM in this paper. The theoretical results obtained closely resemble the practical tests conducted on a low-power-scale vehicle prototype, developed to validate rapid prototyping of the controllers and the energy management systems.

The developed model neglects the phase current dynamics of the machine, reducing the system order. Moreover, the model does not require operations with frequencies higher than 10 Hz (the frequency range of the vehicle load), which allows increasing the sampling step and obtaining fast results

for long driving cycles (over 1,000 s). Thus, increasing the step size extends the task execution time in HIL simulations, making it more effective for real-time prototyping of EMS with complex controllers.

The theoretical results show similarity with the experimental results at mid and higher frequencies. However, due to the TIG's more pronounced parameter variations at low synchronous frequencies, the theoretical results of the model with fixed loss parameters (core losses and rotor resistance) deviate from the practical results, reducing the model's reliability under a wider range of frequency conditions. Consequently, for EMS designs operating at low frequencies, precise determination of TIG parameters is essential, which can be achieved through parameter estimation using a Kalman filter. Finally, with its well-established literature, ease of sensor installation, and extensive familiarity among engineers, the ICE-IG is a viable alternative for low-power scale SHV applications, aiming at lower acquisition costs and facilitating initial project implementation.

ACKNOWLEDGMENT

This work was supported by the Sao Paulo Research Foundation (FAPESP) under grants 2022/00628-9 and 2024/00607-7, the Coordination for the Improvement of Higher Education Personnel (CAPES) under grant 88887.595700/2020-00, the National Council for Scientific and Technological Development (CNPq) under grants 311959/2021-0 and 312664/2021-4 and the Research Development Foundation (FUNDEP) Rota 2030/Line V under grant 27192/27.

AUTHOR'S CONTRIBUTIONS

M. V. R. CAMPOS: Conceptualization, Data Curation, Investigation, Methodology, Project Administration, Software, Validation, Visualization, Writing – Original Draft. **L. J. R. SILVA**: Conceptualization, Data Curation, Investigation, Methodology, Visualization, Writing – Original Draft. **J. W. WANG**: Data Curation, Resources, Validation, Visualization, Writing – Original Draft. **T. P. ALVES**: Data Curation, Resources, Validation, Visualization, Writing – Original Draft. **B. M. ZILLI**: Conceptualization, Investigation, Methodology, Visualization, Writing – Original Draft. **R. V. A. NEVES**: Formal Analysis, Supervision, Visualization. **V. A. OLIVEIRA**: Formal Analysis, Funding Acquisition, Supervision, Visualization, Writing – Review & Editing. **R. Q. MACHADO**: Formal Analysis, Funding Acquisition, Supervision, Visualization, Writing – Review & Editing.

PLAGIARISM POLICY

This article was submitted to the similarity system provided by Crossref and powered by iThenticate – Similarity Check.

REFERENCES

[1] S. L. S. L. Oliveira, J. C. de Freitas Pessôa, L. Cavalcanti, "A atuação do veículo híbrido no mercado brasileiro: análise das oportunidades de inserção no mercado automotivo", *Revista Brasileira de Gestao Ambiental e Sustentabilidade*, vol. 9, no. 21, pp. 317–328, 2022, doi:10.21438/rbgas(2022)092120.

[2] M. V. Campos, L. J. R. Silva, T. A. Fagundes, R. V. A. Neves, R. Q. Machado, V. A. Oliveira, "Average model of bidirectional DC/DC and AC/DC converters coupled in a DC Link for series hybrid electric vehicle", *in 2023 IEEE 8th Southern Power Electronics Conference (SPEC)*, pp. 1–8, IEEE, 2023, doi:10.1109/SPEC56436.2023.10407526.

[3] D. Miao, Y. Mallet, J. Gyselinck, J. Shen, "Wide speed range permanent magnet synchronous generator design for a DC power system", *Chinese Journal of Electrical Engineering*, vol. 3, no. 1, pp. 33–41, 2017, doi:10.23919/CJEE.2017.7961320.

[4] L. J. Ribeiro Silva, M. Von Rondow Campos, T. A. Fagundes, R. V. Alves Neves, R. Q. Machado, V. A. Oliveira, "Mathematical model and control of a three-level boost converter used as electronic interface for fuel cell vehicles", *in 2023 IEEE 2nd Industrial Electronics Society Annual On-Line Conference (ONCON)*, pp. 1–6, 2023, doi:10.1109/ONCON60463.2023.10431338.

[5] M. V. Campos, L. J. R. Silva, T. A. Fagundes, R. V. Neves, J. J. Kalil, R. Q. Machado, "Modelo acoplado de conversores cc-cc bidirecionais para a microrrede cc de um veículo elétrico", *in Congresso Brasileiro de Automática-CBA*, vol. 3, 2022, doi:https://doi.org/10.20906/CBA2022/3276.

[6] T. A. Fagundes, G. H. Favaro Fuzato, R. F. Quirino Magossi, M. Von Rondow Campos, L. J. Ribeiro Silva, R. Q. Machado, "A Novel Dual-Input Cuk-Based Converter: Modeling, Analysis and Design", *in 2023 IEEE 8th Southern Power Electronics Conference and 17th Brazilian Power Electronics Conference (SPEC/COBEP)*, pp. 1–8, 2023, doi:10.1109/SPEC56436.2023.10407956.

[7] M. V. Campos, L. J. R. Silva, T. A. Fagundes, R. V. Neves, J. J. Kalil, R. Q. Machado, "Gerenciamento Inteligente de Energia entre Baterias e Ultracapacitores em Veículos Elétricos Leves com Otimização por Enxame de Partículas", *in Congresso Brasileiro de Automática-CBA*, vol. 3, 2022, doi:https://doi.org/10.20906/sbse.v2i1.3074.

[8] B. Hu, J. Li, "An Adaptive Hierarchical Energy Management Strategy for Hybrid Electric Vehicles Combining Heuristic Domain Knowledge and Data-Driven Deep Reinforcement Learning", *IEEE Transactions on Transportation Electrification*, vol. 8, no. 3, pp. 3275–3288, 2022, doi:10.1109/TTE.2021.3132773.

[9] Y. Hu, W. Li, K. Xu, T. Zahid, F. Qin, C. Li, "Energy Management Strategy for a Hybrid Electric Vehicle Based on Deep Reinforcement Learning", *Applied Sciences*, vol. 8, no. 2, 2018, doi:10.3390/app8020187, URL: https://www.mdpi.com/2076-3417/8/2/187.

[10] M. V. R. Campos, L. J. R. Silva, T. A. Fagundes, R. V. A. Neves, V. A. Oliveira, R. Q. Machado, "Energy Management System based on S-shaped Functions for Series Hybrid Vehicle under a Fully Active Topology", *IEEE Transactions on Vehicular Technology*, pp. 1–16, 2024, doi:10.1109/TVT.2024.3498703.

[11] C.-T. Pan, T.-C. Chen, "Modelling and analysis of a three phase PWM AC—DC convertor without current sensor", *in IEE Proceedings B (Electric Power Applications)*, vol. 140, pp. 201–208, IET, 1993, doi:10.1049/ip-b.1993.0024.

[12] R. F. V. Kan, L. A. Ramos, M. Mezaroba, C. Rech, "Conversor CA-CC trifásico bidirecional e isolado de único estágio para aplicação em carregadores veiculares multifuncionais", *Eletrônica de Potência*, vol. 29, p. e202404, Apr. 2024, doi:10.18618/REP.2024.1.0030, URL: https://journal.sobraep.org.br/index.php/rep/article/view/906.

[13] V. M. Krishna, V. Sandeep, S. Murthy, K. Yadlapati, "Experimental investigation on performance comparison of self excited induction generator and permanent magnet synchronous generator for small scale renewable energy applications", *Renewable Energy*, vol. 195, pp. 431–441, 2022, doi:https://doi.org/10.1016/j.renene.2022.06.051, URL: https://www.sciencedirect.com/science/article/pii/S0960148122008837.

[14] C. E. A. Silva, D. S. O. Jr., H. M. d. O. Filho, L. H. S. C. Barreto, F. L. M. Antunes, "A Three-Phase Rectifier for Wecs With Indirect Current Control", *Eletrônica de Potência*, vol. 16, no. 1, p. 28–36, Feb. 2011, doi:10.18618/REP.2011.1.028036, URL: https://journal.sobraep.org.br/index.php/rep/article/view/392.

[15] A. S. Al-Adsani, N. Schofield, "Hybrid permanent magnet generators for electric vehicle applications", *in 2009 IEEE International Electric Machines and Drives Conference*, pp. 1754–1761, 2009, doi:10.1109/IEMDC.2009.5075440.

[16] R. Q. Machado, S. Buso, J. A. Pomilio, "Sistema de Geração Distribuída Utilizando Gerador de Indução Trifásico e Fontes CC

Conectado a Rede Monofásica", *Eletrônica de Potência*, vol. 10, no. 1, p. 51–58, Jun. 2005, doi:10.18618/REP.2005.1.051058, URL: https://journal.sobraep.org.br/index.php/rep/article/view/689.

[17] R. Figueiredo, I. Oliani, A. S. Lunardi, A. J. Sguarezi Filho, D. Albiero, M. Mezaroba, "Comparação de estratégias de controle preditivo e direto de torque para motores de indução", *Eletrônica de Potência*, vol. 29, p. e202406, Apr. 2024, doi:10.18618/REP.2024.1.0035, URL: https://journal.sobraep.org.br/index.php/rep/article/view/908.

[18] R. B. F. Figueiredo, A. S. Lunardi, A. J. S. Filho, A. Pelizari, "Controle Preditivo Robusto com Conjunto Finito de Estados para Máquinas de Indução", *Eletrônica de Potência*, vol. 27, no. 3, p. 208–215, Aug. 2022, doi:10.18618/REP.2022.3.0027, URL: https://journal.sobraep.org.br/index.php/rep/article/view/71.

[19] B. Tabbache, Y. Aboub, K. Marouani, A. Kheloui, M. Benbouzid, "A simple and effective hardware-in-the-loop simulation platform for urban electric vehicles", *in 2012 First International Conference on Renewable Energies and Vehicular Technology*, pp. 251–255, 2012, doi:10.1109/REVET.2012.6195279.

[20] D.-D. Tran, M. Vafaeipour, M. El Baghdadi, R. Barrero, J. Van Mierlo, O. Hegazy, "Thorough state-of-the-art analysis of electric and hybrid vehicle powertrains: Topologies and integrated energy management strategies", *Renewable and Sustainable Energy Reviews*, vol. 119, p. 109596, 2020, doi:https://doi.org/10.1016/j.rser.2019.109596, URL: https://www.sciencedirect.com/science/article/pii/S1364032119308044.

[21] C. Yang, X. Du, W. Wang, L. Yang, M. Zha, "A Rolling Convergent Equivalent Consumption Minimization Strategy for Plug-in Hybrid Electric Vehicles", *IEEE Transactions on Vehicular Technology*, vol. 73, no. 3, pp. 3340–3353, 2024, doi:10.1109/TVT.2023.3324473.

[22] G. Du, Y. Zou, X. Zhang, L. Guo, N. Guo, "Heuristic Energy Management Strategy of Hybrid Electric Vehicle Based on Deep Reinforcement Learning With Accelerated Gradient Optimization", *IEEE Transactions on Transportation Electrification*, vol. 7, no. 4, pp. 2194–2208, 2021, doi:10.1109/TTE.2021.3088853.

[23] T. J. BARLOW, S. Latham, I. McCrae, P. Boulter, "A reference book of driving cycles for use in the measurement of road vehicle emissions", *TRL Published Project Report*, 2009.

[24] O. Kiselychnyk, M. Bodson, J. Wang, "Comparison of Two Magnetic Saturation Models of Induction Machines and Experimental Validation", *IEEE Transactions on Industrial Electronics*, vol. 64, no. 1, pp. 81–90, 2017, doi:10.1109/TIE.2016.2608766.

[25] V. H. K. Ries, G. Waltrich, A. Vaccari, "Estimativa de Mapa de Eficiência para Máquinas Elétricas Através do Método de Filtro de Kalman Estendido", *Eletrônica de Potência*, vol. 29, p. e202426, Aug. 2024, doi:10.18618/REP.2005.2.061068, URL: https://journal.sobraep.org.br/index.php/rep/article/view/935.

[26] G. Biscardi, L. J. R. Silva, M. V. R. Campos, D. R. Schutz, R. Q. Machado, V. A. Oliveira, "Estimaçao de parâmetros elétricos de motores de induçao trifásicos via métodos de otimizaçao heurısticos", *in Simpósio Brasileiro de Automação Inteligente-SBAI*, vol. 1, 2023, doi:https://doi.org/10.20906/SBAI-SBSE-2023/3796.

BIOGRAPHIES

Márcio Von Rondow Campos was born in Caratinga, Brazil. He received the B.S in electrical engineering in 2022 from the Federal University of Viçosa and the M.S. degree in 2024 from the University of Sao Paulo. He is currently working on his Ph.D. in electrical engineering at the University of Sao Paulo and his mains research interest are in the fields of dc/dc converters for renewable energy sources, microgrids, energy management and hybrid electric vehicles.

Lucas Jonys Ribeiro Silva received the B.S. in electrical engineering in 2020 from The Federal University of Viçosa and the M.S. degree in 2022 from the University of Sao Paulo. He is currently working on his Ph.D. in electrical engineering at the University of Sao Paulo. His main research interest are in the fields of microgrids, electric and hybrid vehicles, energy management and dc/dc converters for renewable energy sources and storage systems.

Jen W. Wang was born in Santa Bárbara d'Oeste, Brazil, in 2000. Currently is a student in Electrical Engineering with an emphasis in Control and Automation at the Federal University of São Carlos. His main research interests are in the fields of microgrids, hybrid vehicles, and energy management.

Thayson Pereira Alves holds the title of Technician in Electrotechnics in the area of Control and Industrial Processes at the Federal Institute of Education, Science and Technology of Maranhão and is currently a student in Electrical Engineering with an emphasis on Energy Systems and Automation at the School of Engineering of São Carlos - USP. He has a Conscious Energy Consumption certificate from the National Industrial Learning Service and his main research interests are in the areas of control and automation engineering.

Bruno Meneghel Zilli received the B.S. in electronic engineering in 2015 from the Federal University of Technology-Paraná and the M.S. degree in Energy in Agriculture Engineering from the Western Paraná State University, 2018. He is currently working on his Ph.D. in electrical engineering at the University of Sao Paulo. His main research interest are in the fields of microgrids, harmonic compensation, energy management and renewable energy sources.

Rodolpho Vilela Alves Neves received the B. S. from the Federal University of Viçosa (UFV), Brazil, in 2011, and the M.Sc. and D.Sc. in Electrical Engineering from the University of Sao Paulo, Sao Carlos, Brazil, in 2013 and 2018, respectively. From 2015 to 2016, he was a Visiting Researcher at Aalborg University, Denmark. He is currently an Adjunct Professor in the Department of Electrical Engineering at UFV. His research interests include intelligent control strategies and modeling dynamic systems.

Vilma Alves de Oliveira (Life Senior Member, IEEE) received the B.Eng. degree in electronics from the Rio de Janeiro State University, Rio de Janeiro, Brazil, in 1976, the M.Sc. degree from the Federal University of Rio de Janeiro, Rio de Janeiro, in 1980, and the Ph.D. degree from the University of Southampton, Southampton, U.K., in 1989, both in electrical engineering. In 1990, she joined the Department of Electrical and Computing Engineering, University of Sao Paulo, Sao Paulo, Brazil, where she is currently a Full Professor. Her research interests include fuzzy control and control design and its applications. Prof. Oliveira is currently the Editor in Chief for the Journal of Control, Automation and Electrical Systems.

Ricardo Quadros Machado (M'2005, SM'2018) received the B. S. from the University of Santa Maria in 1997, the M.S. (2000) and the Ph.D. (2005) degrees in Electrical Engineering from the University of Campinas. From 2002 to 2003 he was a visiting researcher at the University of Padova, Italy and from 2005 to 2007 he was a post-doctorate at the Federal University of Santa Maria, Brazil. From 2013 to 2014 he was visiting professor at the University of Toronto, Canada. Currently, he is associated professor at the University of Sao Paulo and his main research interests are: processing of energy in dc/dc and dc/ac converters, digital control of power converters, distributed generation systems, smart grids and control of renewable energy sources.